

A Convolutional Neural Network Based Framework for Linear Fluid Dynamics

Kwame Agyei-Baah¹, Muhammad Rizwanur Rahman² and E. R. Smith¹

¹Department of Mechanical and Aerospace Engineering, Brunel University of London, Uxbridge UB8 3PH, United Kingdom

² Department of Mechanical and Production Engineering, Islamic University of Technology, Dhaka, Bangladesh

1 Abstract

Fluid dynamics, for its strength in describing physical phenomena across vastly different scales from the cheerios effect on the breakfast table to the evolution of cosmic and quantum systems, has been called the ‘queen mother’ of science (Bush, 2015). However, a central challenge remains: ensuring the generalisability, interpretability and reliability of the machine learned models when applied to physical systems. To address this, we present a transparent approach that provides insights into how data-driven fluids dynamics and machine learning (ML) work. This is achieved by training a convolutional neural network (CNN), on data from a simple laminar fluid flow, to behave as an operator that exactly matches the finite-difference numerics. Importantly, the model demonstrates strong generalisation capability by reproducing the dynamics for a wide range of distinct and unseen flow conditions within the same flow category. The CNN learns the forward Euler three-point stencil weights, capturing physical principles such as consistency and symmetry despite having only three tunable weights. Going beyond pure numerical training (numCNN), the approach is shown to work when trained on analytical (anCNN) and even molecular dynamics (mdCNN) data. In some cases, the physics is not captured, and thanks to the simple and interpretable form, these CNNs provide insight into the limits, pitfalls and best practice of data-driven fluid models. Because the approach is based on finite-difference operators and demonstrated with diffusive flow, it naturally extends to many structured-grid computational fluid dynamics (CFD) problems, including turbulent, multiphase, and multiscale flows.

Keywords: Machine Learning, Numerical schemes, Finite difference, Convolutional Neural networks, Fluid dynamics

2 Introduction

From molten rock flowing in the volcanic eruptions to the quark-gluon plasma within protons and neutrons, and even to the phenomena at the event horizon of a black hole (Tong, 2025), fluid mechanics offer a unifying language to describe how matters flow. At its core, fluid mechanics seeks to understand the motion of liquids and gases, most often through the solution of the Navier–Stokes equations. For decades, computational methods have been employed to solve these equations across a wide range of fluid mechanical problems. However, the application of traditional computational fluid dynamics (CFD) techniques for tackling realistic flows thus particularly those involving complex geometries, chemical agents e.g., surfactants and additives, and the resulting non-linearities, turbulence, or multiphase interactions remains computationally expensive, and hence limited.

Recent advances in machine learning (ML) offer a paradigm shift, with algorithms capable of processing and extracting information from large dataset, automating feature detection and augmenting human domain knowledge (Brunton et al., 2024). Instead of solely relying on solving the governing equations which are limited by their inherent assumptions, and rare to find for the aforementioned complex flows, machine learning offers a new way to handle these problems by finding patterns in data. This way, machine learning can complement traditional fluid mechanical approaches with data-informed predictions, reveal previously uncharacterised non-linearities, and accelerate the discovery of hidden flow-physics. A substantial amount of research in machine learning continues to advance across various disciplines, including healthcare, finance, marketing, and engineering. And the field of fluid mechanics is no exception. Far from being overlooked, fluid mechanics community has witnessed significant progress as researchers increasingly integrate various machine learning techniques to solve complex fluid flow problems.

Vinuesa and Brunton (2022) described rapid advancements in CFD driven by machine learning, highlighting techniques such as proper orthogonal decomposition and autoencoders that help manage the complexity of fluid flow data. In a comprehensive review, Brunton et al. (2024) discussed a variety of frameworks aimed at understanding, modelling, optimising, and controlling fluid flows. Wang et al. (2024) further elaborated these concepts examining techniques such as Physics-Informed Neural Networks (PINNs), Deep Operator Networks (Deep O-Nets), Convolutional Neural Networks (CNNs), and Transformers; all of which are getting increasing acceptance and popularity in computational fluid dynamics. A practical application of machine learning is seen where a firefly machine learning algorithm is used as a deep learning flood forecasting tool for a watershed area in Tennessee, USA (Fordjour, 2024). In particular the introduction of PINNs by Raissi et al. (2019) has attracted considerable attention for their ability to embed the governing equations (PDEs) directly into the neural network’s loss function.

Combining neural networks with the laws of physics promises a paradigm shift in unearthing numerous problems across scales concerning fluid flows. Among numerous investigations in the recent years concerning PINNs, Deng et al. (2023) employed a transformer-based encoder-decoder network for the prediction of transonic flow over supercritical airfoils, ingeniously encoding the geometric input with diverse information points. Shan et al. (2023) focused on turbulence modelling

through data assimilation and machine learning for separated flows over airfoils. Agostini (2020) combined the concept of auto-encoders with other machine learning algorithms in studying the flow behind a cylinder providing a low-dimensional model (a probabilistic flow prediction). Cai et al. (2021) used PINNs framework to tackle a heat transfer problem which cannot be handled by traditional computational methods. Li et al. (2020) used neural operators via graph kernel networks to learn mappings between function spaces, enabling mesh-free generalisation across discretisations. The use of Nyström approximation, enabled efficient handling of unstructured grids that outperformed mesh-dependent neural networks. The method supported sparse data, semi-supervised learning, and geometry transfer; e.g., across airfoil shapes without interpolation.

Raissi and Karniadakis (2018) proposed a framework that relies on Gaussian Process, a powerful tool that is used for probabilistic inference over functions that balances between model complexity and data fitting. This approach is applied to canonical problems including the Navier-Stokes equations, the Schrödinger equation and the time dependent linear fractional equations. Their work (Raissi et al., 2017a,b) facilitated the development of models capable of handling complex domains without requiring large quantities of data.

Initial exploratory investigations in the present study employed artificial neural networks (ANNs) to solve the one-dimensional (1D) heat equation for a range of viscosities as a baseline to understand how neural networks capture flow dynamics. Feature engineering was applied to embed physical information into the model. However, the model's marked failure to predict beyond trained viscosity ranges highlighted the limitations of purely data-driven approaches. To address this, Physics-Informed Neural Networks (PINNs) were explored by incorporating residuals of the 1D heat equation, along with boundary and initial conditions, directly into the loss function. While this improved physical consistency, the model still exhibited instability and failed to generalise reliably beyond the training range, an observation consistent with previous work (Fesser et al., 2023). With a fully converged PINNs architecture, Bonfanti et al. (2024) too obtained accurate predictions only within the immediate proximity of the training domain, and the model poorly performed outside the domain. These underscore a broader gap in the field where most machine learning models for CFD remain tailored to specific flow conditions or geometrical settings, limiting their general applicability. Worse still, the black box nature means we do not know how general our model is.

Hybrid approaches coupling machine learning with traditional numerical solvers despite their potential to enhance accuracy and efficiency in solving complex flows are only at their initial phase of development. This can be seen in Rackauckas et al. (2020b) where the authors proposed a tool for mixing the information of physical laws and scientific models with data-driven machine learning approaches for universal differential equations (UDEs). In addition, a major challenge lies in the interpretability of machine learning models, which are often treated as black boxes without sufficient clarity of the underlying mathematical processes. This issue is elaborated in a comprehensive review by Hassija et al. (2024). To address these challenges, the present study investigates convolutional neural networks (CNNs) an advanced version of artificial neural networks (ANNs) primarily designed to extract features from grid-like matrix datasets (LeCun and Bengio, 1998) and perform image recognition. Similar to artificial neural networks (ANNs), convolutional

neural networks consist of neurons that learn and optimize over time. CNNs are specifically designed for recognizing patterns in images, thus, enabling the integration of image-related features directly into the architecture. This renders CNNs more effective for visual tasks while reducing the number of parameters required for the model (O’Shea and Nash, 2015). Because CNNs require far fewer parameters than fully connected ANNs and their architecture is well suited to grid-structured data, CNNs are a natural choice for this work.

Similar ideas have already been covered in various works, Queiruga (2019) coupled convolutional neural networks with classical numerical schemes for solving spatiotemporal physics problems. Focusing on the 1D heat equation and the inviscid Burgers equation, Queiruga (2019) showed that a single-layer CNN trained on the heat-equation trajectories naturally converges to the traditional finite-difference stencil, whereas a GAN-style (Generative Adversarial Networks) training fails to recover those weights. This work does not appear to have been published in a journal and the idea was not expanded beyond an initial proof of concept. The use of CNNs for numerics represent a subset of more general approaches. Long et al. (2018) introduced PDE-Net, a deep forward neural network that employs convolution kernels to predict complex system dynamics and to uncover the underlying PDE models, learning differential operators alongside the non-linear response functions. Rackauckas et al. (2020a) proposed universal differential equations (UDEs) as a unifying framework, demonstrating their use on the one-dimensional Fisher–KPP equation with CNNs acting as learnable stencils. More recently, Kim and Choi (2022) showed that a CNN kernel based on the five-point finite difference stencils can learn numerical schemes with limited data while achieving low relative errors. The existing methods of preserving symmetries in fluid dynamics such as rotation invariance, translation invariance, or using equivariant CNNs where convolutional layers automatically encode the desired symmetry are discussed by Zhang et al. (2025).

The aforementioned works motivate the present study, which adopts convolutional neural networks in their simplest form to integrate machine learning into fluid dynamics through finite-difference numerical schemes. In doing so, we directly link to years of finite difference theory development (Hirsch, 2007); explicitly linking CNN architectures to the mathematical progression from $u^t \rightarrow u^{t+1}$. This approach, schematically illustrated in Fig. 1, aims to bridge the gap between data-driven models and the fundamental mechanisms of fluid dynamics, providing a more transparent alternative to treating ML purely as a black box. This is then extended beyond purely matching the finite difference stencils to use these CNNs as numerical stencils which match both analytical and even molecular dynamics data. This provides a technique which has elements of physics discover similar to techniques like sindy (Brunton et al., 2024), which can allow solution to the inverse problem (Ambarzumian, 1929) all while giving a ML trained model completely grounded in finite difference theory.

The remainder of the paper is organised as follows. Section 3 presents the methodology, including the governing equations, the CNN architecture, and the training procedure. Section 4 reports the results and offers a detailed discussion of models trained on numerical and analytical data, ending with an application of the CNN kernel learner to molecular dynamics data that provides additional insight. Finally, Section 5 summarises the findings and concludes the paper.

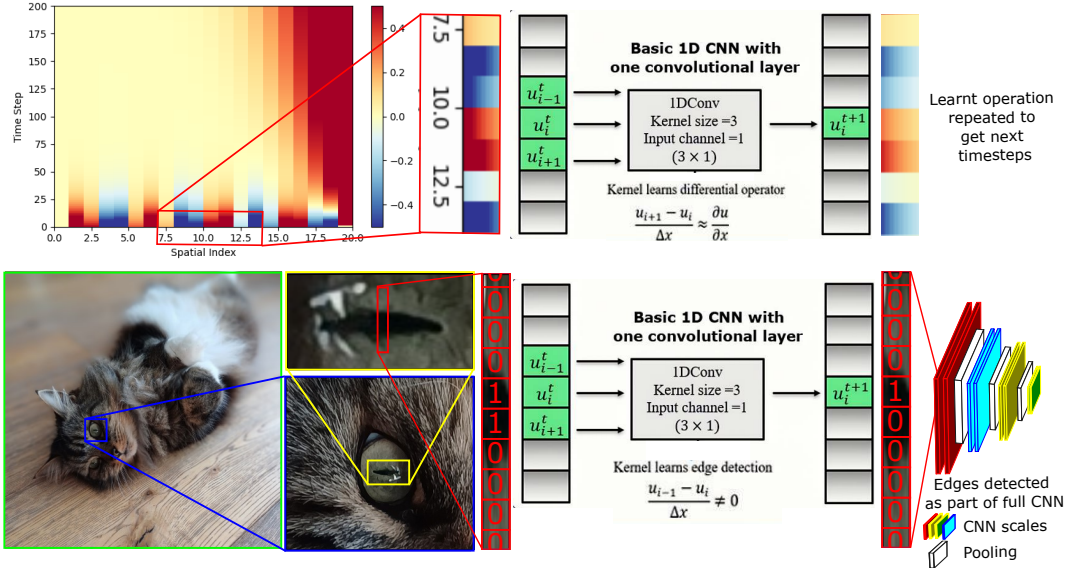


Figure 1: Top panel illustrates the architecture of a 1D CNN and how CNN operation can be likened to a Forward Euler 3 point (FE3) stencil with respect to $u^t \rightarrow u^{t+1}$. The bottom panel shows how CNNs use convolution similar to the FE3 stencil which learns the differentiation operator as a form of edge detection in image processing.

3 Methodology

3.1 The 1D heat equation

This study uses two classical fluid flow problems, (i) Couette flow, and (ii) Stokes' second problem, to train and test a machine learned algorithm. Both of these wall driven fluid flows can be described by the one dimensional partial differential equation, most commonly known as the heat equation, or the diffusion equation,

$$\frac{\partial u}{\partial t} = \mu \frac{\partial^2 u}{\partial x^2}. \quad (1)$$

The dependent variable u represents temperature for heat conduction problems, whereas, it denotes velocity field for wall-driven flows, μ is thermal diffusivity (heat conduction) or the dynamic viscosity (wall driven flow), and x is the spatial position. The present work considers wall driven flows, and as illustrated in Figure 2 (a), in the case of Couette flow, an initial condition u_0 with either the top $tBC = u_t$ or the bottom $bBC = u_b$ wall boundary slides with a constant velocity, whereas, for Stokes' second problem, the wall oscillates as a sinusoid with frequency, ω along the x direction.

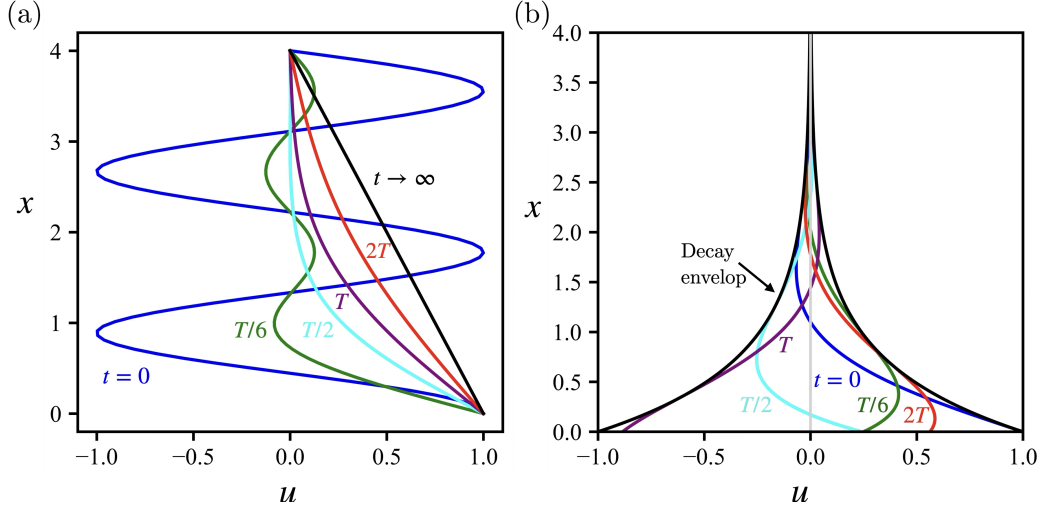


Figure 2: Illustrations of two cases studied: (a) Wall-driven flow (Couette flow) and (b) Stokes' second problem. Simulation parameters for cases (a) and (b): $\mu = 0.02$, $\Delta t = 0.1$, $L_x = 4.0$, $n_x = 80$, total time $T = 5000 \Delta t$. Profiles at $t = \{0, T/6, T/2, T, 2T\}$ are shown for both cases. (a) Wall-driven flow: top wall moves in $+x$ with $U_0 = \sin((1.125x + 0.5)\pi)$; boundary values $u(0) = bBC = 1$, $u(L_x) = tBC = 0$. Curve labeled $t \rightarrow \infty$ is the steady Couette solution. For the Stokes' second problem in panel (b), $\omega = 1$ and $\kappa = 0.7$.

3.2 Analytical Solutions

As such, Eq. (1) gives either Couette flow or Stokes' second problem based on the boundary conditions.

When the flow is driven by the sliding velocity of one of the walls (Couette flow), the analytical solution is given by

$$u(x, t) = u_{\text{steady}}(x) + \sum_{n=1}^{\infty} A_n \sin(\beta_n x) e^{-\mu \beta_n^2 t} \quad (2)$$

where $u_{\text{steady}}(x) = u_b + (u_t - u_b)x/L$, the coefficient $A_n = \frac{2}{L} \int_0^L [u_0(x) - u_{\text{steady}}(x)] \sin(\beta_n x) dx$ and wavelength is denoted as $\beta_n = (n\pi)/L$. Whereas, for the flow field resulting from the oscillation of the bottom wall $u(x = 0, t) = u_b(t) = U \sin(\omega t)$ (Stokes' second problem) and assuming an open top so $u(x \rightarrow \infty, t)$, the analytical solution takes the form,

$$u(x, t) = u_b \sin(\omega t - \kappa x) e^{-\kappa x}, \quad (3)$$

where $\kappa = \sqrt{\omega/(2\mu)}$ and U is the wall oscillation magnitude. In practice, the top wall is actually a fixed boundary but the domain is taken to be large enough to minimise the effect of this.

3.3 Numerical Solution

The diffusion (or, heat) equation is discretised to mimic the setup of a convolution kernel. One of the simplest discretised form of (1) uses the forward Euler in time and a 3-point stencil in space,

$$\frac{u_i^{t+1} - u_i^t}{\Delta t} = \mu \left[\frac{u_{i+1}^t - 2u_i^t + u_{i-1}^t}{(\Delta x)^2} \right], \quad (4)$$

Taking $C = \mu\Delta t/(\Delta x)^2$ this is rearranged to,

$$u_i^{t+1} = u_i^t + C (u_{i+1}^t - 2u_i^t + u_{i-1}^t). \quad (5)$$

The parameters used for the majority of simulations presented in this work are as follows, unless otherwise stated: dynamic viscosity, $\mu = 0.02$, timestep, $\Delta t = 0.10$ with a spatial grid, $n_x = 20$ for a domain length, $L_x = 4.0$ so a spatial resolution of, $\Delta x = L_x/(n_x - 1) = 0.2105$ over $N_t = 200$ timesteps which gives $C = 0.045125$. We consider 3 conditions used to construct the numerical scheme in Eq. (4) for the diffusion operator (Hirsch, 2007), where in general,

$$\frac{\partial^2 u}{\partial x^2} \approx b_1 u_{i+1}^t - b_0 u_i^t + b_{-1} u_{i-1}^t. \quad (6)$$

Here, $b_1 = 1/(\Delta x)^2 = b_{-1}$, $b_0 = 2/(\Delta x)^2$, and the coefficients are obtained from,

$$\mathcal{A}_1 = \sum_{i \in \{-1, 0, 1\}} b_i = 0 \quad (\text{consistency}) \quad (7a)$$

$$\mathcal{A}_2 = \sum_{i \in \{-1, 0, 1\}} i b_i = 0 \quad (\text{symmetry}) \quad (7b)$$

$$\mathcal{A}_3 = \sum_{i \in \{-1, 0, 1\}} i^2 b_i - 2C = 0 \quad (2 \times \text{CFL condition}) \quad (7c)$$

Solving these three equations for 3 unknown weights yield values of $b_{-1} = C$, $b_0 = -2C$, $b_1 = C$ which is consistent with Eq. (5) above. These can be written as a vector $\mathbf{b} = b_i = [C, -2C, C]$ and written in C independency form by defining $\tilde{\mathbf{b}} = \mathbf{b}/C = [1, -2, 1]$. These correspond to physical requirements for the kernel, with consistency Eq. (7a) ensuring that in the limit of zero volume, the kernel recovers the continuous differential operator. The symmetry condition of Eq. (7b) guarantees that no diffusion or numerical advection exists in a preferential direction, and the final condition Eq. (7c) confirms stability of the solution. Stability is normally expressed as an upper bound, with the requirement that $\mu\Delta t/\Delta x^2 < 1/2$. The explicit FTCS scheme for the 1D diffusion equation is conditionally stable under the CFL restriction $\mu\Delta t/\Delta x^2 < 1/2$ (Hirsch, 2007). This section has introduced the forward Euler 3-point schemes (denoted as FE3). Higher order spatial and temporal numerical schemes were also studied and are outlined in Appendix A. These include a spatially higher order schemes with 5 point stencil using the forward Euler (FE5) and the multiple time-step Adam-Bashforth for a 3-point stencil (AB3) and a 5 point stencil (AB5).

3.4 Molecular Dynamics

Alongside the analytical and finite difference schemes to solve the diffusion equation, we employ molecular dynamics (MD) simulations to obtain an independent solution of the diffusion process described by Eq. 1 directly. Despite MD being a more fundamental model which depends only on the validity of Newton’s law $\mathbf{F}_i = m\mathbf{a}_i$ for a system of N interacting molecules, this has been shown to reproduce the equations of fluid dynamics on average (Rapaport, 2004). The chosen setup uses a simple Lennard Jones potential $U(r_{ij}) = \epsilon[(\sigma/r_{ij})^{12} - (\sigma/r_{ij})^6]$, with tethered thermostatted wall sliding to drive flow (Todd and Daivis, 2017). This reproduces the continuum diffusion process as shown in Figure 3. The velocity was obtained by an averaging process, binning the domain into 32 cells and averaging the velocity of the molecules over 10 successive timesteps. The viscosity is an output of the simulation, with the only empirical assumption in MD being the choice of intermolecular potential, as a result MD is an excellent way to test the validity of the CNN training approach as it provides an experimental-like setup where the fitted equations only approximate the true physics. The flow fields obtained from MD inherently include noise, to reduce this noise, we chose a relatively large system (with $N = 619,885$ molecules). The simulation was run with Flowmol, which has been extensively validated in previous work (Smith, 2013). The setup is similar to Smith et al. (2019), and readers are referred to this work for further details. In reduced units, the walls were given a density of $\rho_{\text{wall}} = 1$, while the fluid was setup by randomly removing atoms to reach a density of $\rho_{\text{fluid}} = 0.8$ corresponding to the density of liquid argon at $\sim T = 0.8$ in coexistence with its vapor phase (NIST, accessed: 2026-01-05). A Weeks–Chandler–Andersen (WCA) cutoff was used for computational efficiency, with $r_c = 2^{1/6}$. Averaging cells are $\Delta y = 1.44$ with total domain $L_y = 46.03$ in the wall normal direction (*c.f.* the x axis used in continuum treatment which is 1D), and the size of the full domain in other directions, i.e., $\Delta x = L_x = 126.99$ and $\Delta z = L_z = 126.99$. The tethered walls have a width of $L_{\text{wall}} = 4$ at both the top and bottom boundaries, with the topmost and bottommost three cells of the domain treated as wall cells. This means the outer $3\Delta y = 4.3$ of the domain is a wall, which assumes a small region of stick-slip near the wall and gives a good comparison for the middle 26 cells compared to the analytical solution in Figure 3. The outer portions of both the walls, each of width $L_{\text{therm}} = 2$ were thermostated, comprising approximately $N_{\text{therm}} \approx 65,000$ atoms in total. Temperature control was achieved using a Nosé Hoover thermostat with a heat bath coefficient of strength $Q = N_{\text{therm}}\Delta t_{MD}$ where $\Delta t_{MD} = 0.05$ is the MD timestep. Walls are tethered with an anharmonic potential from Petracic and Harrowell (2006) with $k_4 = 5,000$ and $k_6 = 5,000,000$ in $\phi_i(\mathbf{r}_i) = -k_4(\mathbf{r}_i - \mathbf{r}_i^{eq})^4 - k_6(\mathbf{r}_i - \mathbf{r}_i^{eq})^6$ where \mathbf{r}_i^{eq} is the equilibrium position of the tethering site. The top wall was assigned a sliding velocity of $u_{\text{wall}} = 1$ applied to both the atoms and the tethering sites.

The MD system was first equilibrated for 20,000 timesteps with wall thermostating. This equilibration phase preceded the velocity rescaling in the 26 fluid bins to match an initial sinusoidal solution, and the activation of the sliding motion of the top wall. Velocity rescaling was implemented by applying a small correction to all the molecules in the bin proportional to the difference between the instantaneous and the target velocities; consequently the system tempera-

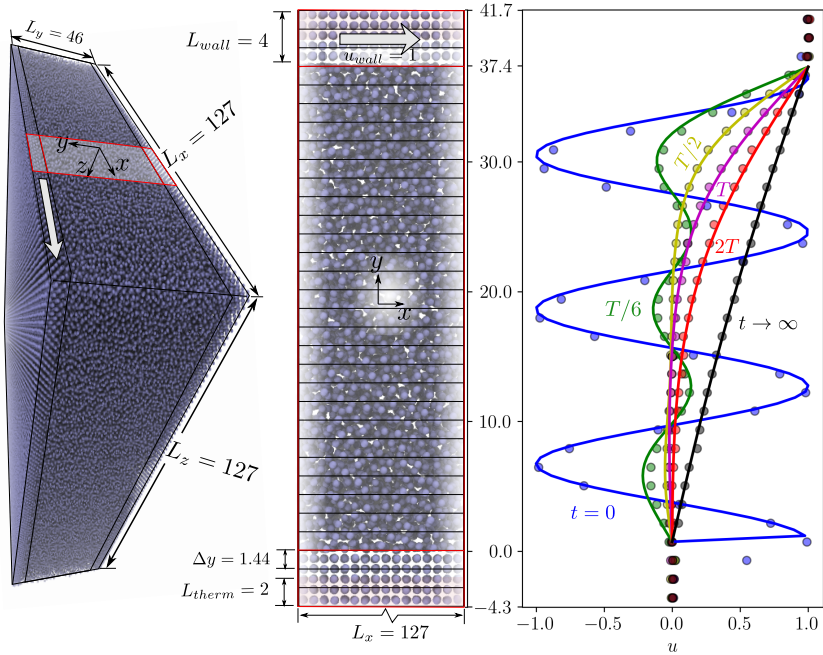


Figure 3: A perspective view of the full MD system is illustrated in the left panel, with the red box shown in the middle highlighting the region used in the schematic, where the corresponding MD cells line up with the velocities (symbols) on the plot on the right at a range of times as multiples of $T = 400\Delta t$ compared to the analytical solution (lines). The start of the fluid domain is shown as zero to match the analytical solution with 3 MD cells below and 3 above. The analytical solution is matched to the MD fluid part in y with $L_{y,fluid} = 37.4$, with half cell $\Delta y = 1.44$ extra at top and bottom and $\mu = 2.14$ with lines plotted at the same times in reduced units.

ture remained unchanged. This rescaling, however, results in a minor jump between molecules in adjacent cells. The applied velocity correction per atom despite being negligible, their cumulative effect might explain the slightly larger effective viscosity seen in the $T/6$ case of Figure 3. After sufficient equilibration of the system, the production run was commenced over 57,000 steps with $\Delta t_{MD} = 0.005$. During this phase, statistics were collected upon averaging data over 10 steps giving 5700 MD snapshots in time, i.e., output times are each separated by $\Delta t = 0.05$. All data generated through the MD simulations, and the source codes to reproduce them are included along with other required scripts for the numerical modelling, as well as for the CNN model.

3.5 The CNN model

The operation of getting the next timestep from the previous one can be expressed using a convolution kernel of size 3, e.g., $\mathbf{k} = [k_{-1}, k_0, k_{+1}]$. Denoting the diffusion kernel as $\mathbf{k}_D = [C, -2C, C]$,

and the identity kernel as $\mathbf{k}_I = [0, 1, 0]$, Eq (5) can be rewritten in convolution form as:

$$u_i^{t+1} = \mathcal{F}_k(u_i^t) = (k_D * u^t)_i + (k_I * u^t)_i = (k * u^t)_i, \quad (8)$$

where ‘*’ denotes the discrete convolution operator, as such $(k * u^t)_i = k_{-1}u_{i-1}^t + k_0u_i^t + k_{+1}u_{i+1}^t$. To be consistent with the numerical operator in Eq. (5), the learned kernel, \mathbf{k} is expected to converge to $[C, 1 - 2C, C]$. This corresponds to the diffusion kernel \mathbf{k}_D learning the weights from the numerical schemes described in section 3.3, such that $\mathbf{k}_D \rightarrow \mathbf{b}$ which, when added to the identity kernel \mathbf{k}_I , yields the full update kernel. In this way, the learnt kernel operator obtains the next timestep of a velocity field from the current one. We define the kernel normalised by C as $\tilde{\mathbf{k}}_D = \mathbf{k}_D/C$.

To train the machine-learned CNN model for the flow fields of interest here, the same approach was followed for all cases, differing only in the dataset used for training the model. The first set of training data were obtained from the corresponding numerical solutions, resulting in the *numerically trained CNN* (abbreviated as numCNN). The second set of data is the exact analytical solutions of Equations (2) and (3), yielding the *analytically trained CNN* (henceforth, abbreviated as anCNN). Since both the analytical and the numerical dataset must be generated by solving Eq. (1) either as an exact analytical solution of the PDE in terms of closed form functions, or as the numerical approximation; we employ a third dataset to examine the robustness of the CNN. This aims to have training dataset which is fundamentally different from the continuum approaches. This MD system has no link to the continuum equation (1) other than through the observation that the average resultant behaviour of unsteady Couette flow in an MD system broadly matches the continuum one (Smith, 2013). The CNN trained on the dataset generated by these MD simulations is abbreviated as mdCNN.

The CNN architecture is identical in all the three cases, anCNN, numCNN, and mdCNN; the only distinction lies in the dataset on which it is trained. In this setup, the CNN effectively learns the numerical stencil weights of explicit time-integration schemes for the wall-driven flow. For numCNN, this is exactly reproducing the numerical scheme, as the CNN is mathematically identical to a finite difference operator. For the anCNN and mdCNN, the resulting CNN stencil is an effective numerical operator that reproduces that data. Using the Adam optimizer, the network iteratively adjusts its initially assigned random weights to minimize the loss. Through back-propagation, the CNN progressively captures the underlying flow physics, and converges to kernel weights that are consistent with the target solutions or weights. The CNN is used as a numerical operator employing a one-dimensional convolutional layer, with the kernel size determined by the chosen finite-difference scheme. Four schemes are considered for solving Equation (2): forward Euler with (i) a 3-point stencil (FE3), and (ii) a 5-point stencil (FE5), and Adams–Bashforth with (iii) a 3-point stencil (AB3), and (iv) a 5-point stencil (AB5).

The kernel is of a length consistent with the finite-difference stencil. The bottom and top boundary conditions (henceforth, referred to as bBC and tBC respectively) are enforced at every timestep. This is done by setting the first ($x = 0$) and last ($x = l$) spatial points of the discrete flow field to the fixed values of the bBC and tBC, with higher order stencils needing special treatment,

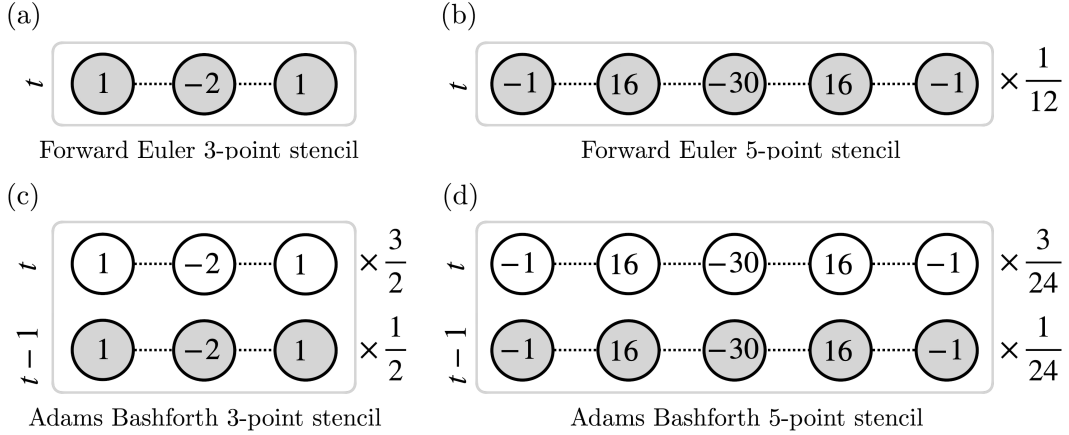


Figure 4: Time-integration stencils and their coefficients: (a) Forward Euler uses a 3-point stencil, $[1, -2, 1]$ and (b) a 5-point stencil, $[-1, 16, -30, 16, -1]$ finite-difference scheme. The 3-point versions are second-order accurate in space, whereas, the 5-point versions achieve fourth-order spatial accuracy. The multistep Adams–Bashforth employs analogous (c) 3-point, and (d) 5-point stencils, which offers second order temporal accuracy

detailed in Appendix A. This way, the boundary conditions are built into the convolutional operation, and do not need to be learnt from the data or require PINNs enforcement. The convolution operation applies the weighted sum to each point and its neighbouring ones, enforcing the finite difference update rule. The other numerical schemes (FE5, AB3, AB5) examined in this study are detailed in Appendix A.

3.5.1 Training

In this section, a separate convolutional neural network (CNN) kernel learner for the four numerical-scheme operators introduced in section 3.5 is implemented. The weights for the numerical schemes considered are shown in Fig.4. The weights of the CNN kernel learners are randomly initialised; there was no clear convergence or stability advantage found in using common methods such as Xavier Initialization (Glorot) method (Glorot and Bengio, 2010). This random initialisation prevents the models from being biased toward the target values at the outset. Once initialised, training proceeds with the Adam optimizer (Kingma and Ba, 2014), with a learning rate of 10^{-3} and a weight decay of zero. All codes are written in python, version 3.10 and Pytorch 2.8 with CUDA 12.6. Model accuracy is assessed by computing the mean squared error (MSE, denoted as ℓ) between the target value at the next timestep and the current prediction using weights k in the

convolutional operator \mathcal{F}_k defined in Eq (8),

$$\ell(u_i^t, u_i^{t+1}) = \frac{1}{n_x N_t} \sum_{t=1}^{N_t} \sum_{i=1}^{n_x-1} \left[\mathcal{F}(u_i^t) - u_i^{t+1} \right]^2 + \sum_{n=1}^3 \lambda_n \mathcal{A}_n. \quad (9)$$

This is minimised over the entire spatial domain ($n_x - 2$ as the outer two points enforce the boundaries) and for all time steps in the simulation to get the value of \mathbf{k} . This training can also be extended to multiple cases by simply defining the loss function over multiple cases (batches) where matched u_i^t and u_i^{t+1} pairs can be shuffled for a wide range of Couette and Stokes' flows with varying boundaries. Note that Eq (9) and the convolution operator can be generalised to take multiple previous timesteps (e.g. u_i^{t-1}) in multi-step schemes like Adam-Bashforth or to predict multiple future steps by recursively applying the \mathcal{F}_k operator. For presentational simplicity, these are not shown here.

The CNN model can be trained with physics constraints using the PINNs approach: the constraint \mathcal{A}_n from equations 7a, 7b and 7c normalised by C , $\tilde{\mathcal{A}}_i = \mathcal{A}_i/C$, yielding,

$$\tilde{\mathcal{A}}_1 = \sum_{i \in \{-1,0,1\}} \tilde{k}_{Di} = 0; \quad \tilde{\mathcal{A}}_2 = \sum_{i \in \{-1,0,1\}} i \tilde{k}_{Di} = 0; \quad \tilde{\mathcal{A}}_3 = \sum_{i \in \{-1,0,1\}} i^2 \tilde{k}_{Di} - 2 = 0 \quad (10)$$

which can be enforced during training via a Lagrange multiplier λ_n . These multipliers weight the constraint terms and are added to the loss in (9), so the total loss equals the data loss plus the three Lagrange-weighted constraint terms; tuning λ_n strengthens or relaxes each physical condition. The effect of the magnitude of these Lagrange multipliers is studied in the Appendix figure A1, but are often chosen as zero so the constraints are not applied in general. Where PINNs is applied, these will be discussed in the various results.

4 Results and Discussion

This section starts by training the CNN on a numerical reference case in section 4.1, with model weights shown to match the expected numerical stencil, giving results which generalise both to new boundary conditions and to Stokes' flow. This reference case is then used as the starting point to train the CNN on the analytical data in section 4.2. This solution is not the same as the numerical model, showing specialisation for the reference case it was trained on. As a result, CNNs are trained on a range of other boundary and initial conditions analytical case, using energy maps to understand the convergence behaviour. Finally, multi-case training is shown which reproduces the same general numerical CNN values. A comparison between numCNN and anCNN is discussed in section 4.3 before exploring the process of training the CNN on MD data in section 4.4.

4.1 numCNN: CNN Trained on Numerical Data

A wide range of boundary and initial conditions were run and analysed, training the CNN kernel learner on numerical solutions, with the resulting weights mostly converging to the same value. To

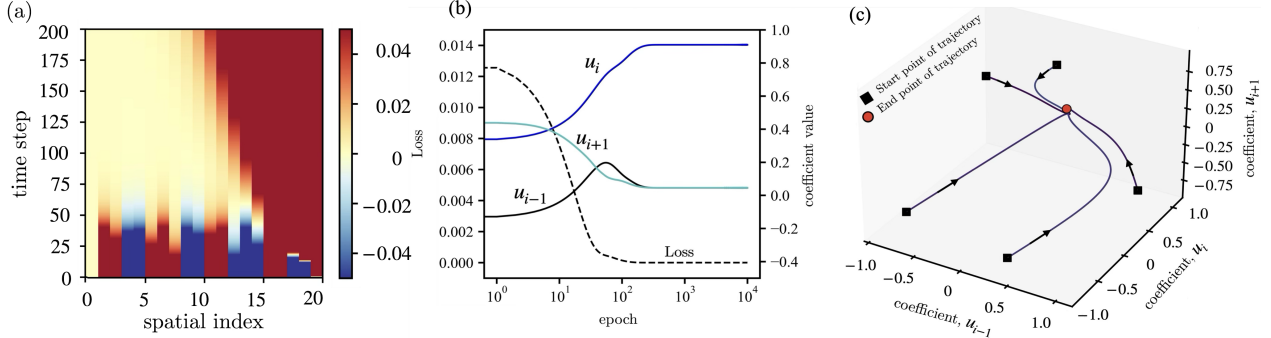


Figure 5: (a) The contour plot shows the reference case studied here with initial condition : $u_0 = \sin(2\pi x)$ with boundary conditions, $bBC = 0$ and $tBC = 1.0$ trained on numerical solution (b) Training loss (left y -axis) and coefficient values for u terms showing expeceted values $\mathbf{k} \rightarrow [0.0451, 1 - 0.0902, 0.0451]$ (right y -axis) for 3-point Forward Euler kernel, (c) Evolution of training trajectories for 5 randomly initialised weights. For all these cases, parameters used for the reference case simulations are: $\mu = 0.02$, $\Delta t = 0.1$, $n_x = 20$, $L_x = 4.0$, $N_t = 200$, $bBC = 0.0$, $tBC = 1.0$ & $u(x, 0) = \sin(2.0\pi x)$,

exemplify this typical behaviour, we chose a reference case with $u(0, t) = 0$, $u(L, t) = 1.0$, $u(x, 0) = \sin(2.0\pi x)$, with numerical results shown in fig.5a using the standard simulation parameters with viscosity $\mu = 0.02$, spatial points $n_x = 20$, domain size $L_x = 4.0$ and timesteps $N_t = 200$ of size $\Delta t = 0.1$. The dataset for the training are generated through CFD simulations utilizing Eq. (5). Fig.5a is a contour plot representation, i.e. spatial and temporal plot of this reference case showing the velocity over the entire training data set.

Since the learned weights from the trained CNN model can be compared with the known numerical operators, the model becomes an interpretable numerical solver instead of a ‘black box’. We show the CNN recovers the target stencil coefficients during training. Figure 5 (b) shows the training loss and the coefficient values for the three-point Forward Euler (FE3) kernel. The loss rapidly decreases by nearly 10^{-15} , while the three learnt coefficients converge to the corresponding finite-difference weights. Figure 5 (c) illustrates the trajectories of the coefficient vectors in the (u_{i-1}, u_i, u_{i+1}) space. Each trajectory begins with a randomly assigned weight vector (black square) but, irrespective of the initialisation, converges to the target FE3 coefficients. The target weights for the diffusion operator are: $\mathbf{k}_D = [0.045125, -0.09025, 0.045125]$ (recall $C = 0.045125$), whereas the learned weights are $[0.04512625, -0.09024877, 0.04512625]$. These weights are written in terms of $\tilde{\mathbf{k}}_D$ which is scaled by C in table 1.

Having established that the CNN successfully identifies the correct stencil weights for a three point stencil, we evaluate how accurately the model recovers the underlying flow solutions for other numerical operators. Table 2 presents the mean-squared error (MSE) for a variety of finite-difference schemes, including a larger spatial stencil with the 5 point scheme, and the multi-timestep Adam-Bashforth technique. These are compared with the CNN-learned diffusion kernel

Target Weight ($\tilde{\mathbf{b}}$)	Learned Weight ($\tilde{\mathbf{k}}_D$)	MSE (ℓ)	$\mathcal{O}(w_{\text{target}} - w_{\text{learned}})$ $\equiv \mathcal{O}(\mathbf{b} - \mathbf{k}_D)$
1	1.00002768		10^{-8}
-2	-1.99997274	$\mathcal{O}(10^{-12})$	10^{-9}
1	1.00002768		10^{-8}

Table 1: Comparison of target and learned weights for single-case 3-point stencil for numCNN, with MSE over the entire $N_t n_x$ domain of reference case in fig 5a.

Scheme	$\mathcal{O}(w_{\text{target}} - w_{\text{learned}})$
Forward Euler 3-point	$10^{-8}, 10^{-9}, 10^{-8}$
Forward Euler 5-point	$10^{-6}, 10^{-5}, 10^{-6}, 10^{-6}, 10^{-6}$
Adams–Bashforth 3-point	$10^{-4}, 10^{-3}, 10^{-7},$ $10^{-4}, 10^{-3}, 10^{-5}$
Adams–Bashforth 5-point	$10^{-4}, 10^{-4}, 10^{-4}, 10^{-6}, 10^{-7},$ $10^{-4}, 10^{-4}, 10^{-4}, 10^{-5}, 10^{-8}$

Table 2: Difference between the target and the learned weights for different finite difference schemes.

(k_D), where the kernel structure is adapted to the corresponding numerical scheme: e.g., a five-point spatial stencil k_i with $i \in \{-2, -1, 0, 1, 2\}$ for the higher-order finite difference scheme, and a three-point spatial and two-point temporal stencil with k_i^t with $i \in \{-1, 0, 1\}$ and $t \in \{-1, 0\}$ for the third-order Adams–Bashforth scheme. It is clear from the error magnitudes that each of the numerical schemes (CNN) model yields results that closely matches the original finite difference solution in table 2. Notably, the FE3 numerical scheme consistently exhibits the lowest error across all weight configurations.

The training results demonstrate that the CNN-based kernel learner successfully recovers the stencil coefficients for all four numerical schemes when trained on their finite-difference solutions. For all the schemes tested in this work including Forward euler 5-point (FE5) and Adams–Bashforth (AB3 and AB5) the CNN accurately recovers the weights. It is worth noting that when the 5 point Euler learner (FE5) is trained on numerical data generated from a lower order scheme, for example data generated from a 3 point forward Euler (FE3) numerical method, it identifies only the three weights reproducing the stencil, i.e. $\tilde{\mathbf{k}}_D \approx [0, 1, -2, 1, 0]$. This appears to be a demonstration of the lottery ticket hypothesis even in a small model (da Cunha et al., 2022), in that for a model given more weights than required, the relevant subset of the weights eventually train as required to capture the physics. The matching to various numerical schemes and even identification of simpler solutions highlights the robustness of these kernel learners.

4.1.1 numCNN applied to unseen flow conditions

To demonstrate how the trained model performs on unseen flow conditions, we adopted two strategies. First, the model was tested on data from Couette flow, with the boundary conditions swapped/inverted as compared to the training data. The second test involved a time varying boundary condition, i.e., Stokes' second problem. Such condition is totally outside the training domain, and represents a stringent test of the generalisation of the numerical scheme. We elaborate the observations from these tests below. Although the agreement presented here is not unexpected, the exact reproduction of the numerical weights means we know the solver is already fully generalised; these tests emphasise this here and set out the methodology moving to the analytical case in section 4.2.

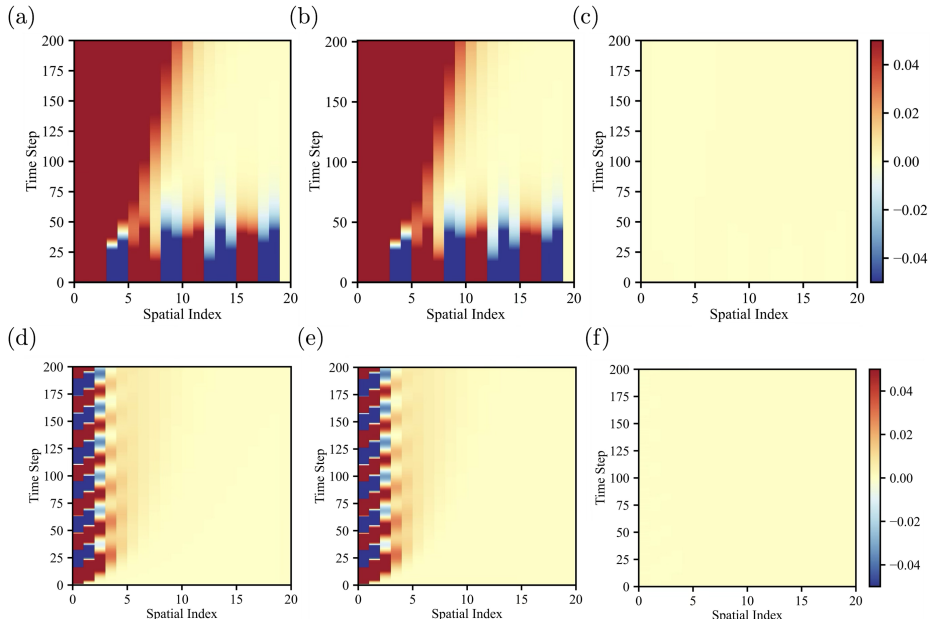


Figure 6: Performance of numerically trained kernel (numCNN) under swapped boundary conditions. Top panels represent Couette flow (a) CNN solution, (b) finite difference solution. Bottom panels show results for Stokes' second problem where (d) is obtained from the CNN model, and (e) from the finite difference scheme. Panels (c) and (f) illustrates the difference between the CNN solution and the numerical solution for each of the cases. The simulation parameters used here are: $\mu = 0.02$, $\Delta t = 0.1$, $n_x = 20$, $L_x = 4.0$, $N_t = 200$, $\Delta x = L_x/(n_x - 1)$. Couette flow: $bBC = 1.0$ & $tBC = 0.0$ and its initial condition is $u_0 = \sin(2.0\pi x)$. Stokes second problem: Boundary conditions – $u(0, t) = \sin(\omega t)$ with $\omega = 2.0$, and $u(L_x, t) = 0$

Couette flow with swapped boundary conditions: The model trained on the data of Couette

flow with top wall sliding (BCs: $[0,1]$), is tested against similar Couette flow but with the bottom wall sliding and the top wall fixed (BCs: $[1,0]$). Recall boundaries are embedded in the training data, not the model so any changes test the weights are not skewed. The solution produced by the numCNN is shown in Fig. 6 (a-c), with the direct numerical solution shown in panel (b). A comparison of these two solutions can be seen from the error plot (panel c) which confirms nearly an absence of any difference between the direct numerical solution, and the solution from the CNN model. This indicates that the learned kernel reproduces the numerical scheme’s behavior without any considerable error, and is robust to this boundary-condition swap, reinforcing the numCNN’s generality under the tested conditions. The advantage becomes particularly evident when the flow field spans many combinations of the parameter space. Once trained under a specific condition, numCNN generalises well to different combinations of the boundary-conditions. This highlights its potential as an efficient and computationally inexpensive alternative, without compromising the accuracy obtained from conventional numerical methods.

Stokes’ second problem: To test the model’s efficacy in solving related but unseen flow conditions, we test the CNN model (which is trained on Couette flow) with Stokes’ second problem. Although both the Couette flow and the Stokes’ second problem belong to the same class of viscous flows, their solutions are distinctly different, and involves different physical characteristics. The CNN’s learned weights, as in Fig. 6 (d) shows excellent agreement with those obtained from the direct numerical solution, as in panel (e). The difference between the two solutions is shown in panel (f) reaffirming the agreement. This demonstrates that even for unseen boundary conditions yielding distinct type of flow fields than the training data, the CNN model can serve as an efficient solver.

4.1.2 Beyond the black box

The robust agreement of figure 6, underscores the capability of the CNN framework to reproduce classical finite-difference coefficients directly from data, i.e., successfully learning the finite difference operators. This exercise demonstrates that CNN functions as a numerical operator capable of capturing the flow physics which are as fully general as the numerical methods they are trained on. Crucially, the clear link from CNN to differential operator provides an interpretable route to overcoming the black-box limitation. We now transition from working with known weights to attempt to match the exact solution.

4.2 anCNN: CNN Trained on Analytical Data

Section 4.1 discussed a CNN model trained on the dataset obtained from numerical solutions of wall driven flows. However, numerical modelling is an approximation of the true analytical solution, with each order of stencil getting closer to the exact solution. It is only in the limits of vanishingly small spatial and temporal step sizes or an infinite order stencil of points, that strict equivalence between the two is attained. Data obtained from the exact solution avoids the truncation and

time integration errors associated with solving the PDE's. As such, a natural benchmark for the numCNN is to compare it against a CNN trained on data obtained by discretely solving the analytical solution. In practice, most fluid flow problems do not admit closed form exact solutions due to the complexities in the underlying partial differential equations necessitating reliance on numerical schemes. Therefore, in this section, we train the CNN on analytical solutions, starting with the reference case used in the introduction of Section 4 which allows us to compare, and evaluate the robustness and correctness of the learned CNN operator compared to the numerical model.

4.2.1 Reference case: $u(0, t) = 0, u(L, t) = 1.0, u(x, 0) = \sin(2.0\pi x)$

The color map in Fig. 7 (a) shows the fluid velocity at different space-time coordinates obtained from the exact solution for Couette flow in this reference case. Subtracting the CNN-predicted flow fields from the exact solution yields the error plots, these are illustrated in, Fig.7 respectively for (b) CNN-trained on analytical data, and (c) CNN-trained on numerical data at every timestep. The color bar ranges from blue at early times to yellow at the final timestep, with intermediate shades indicating the temporal progression. For anCNN (panel b), the errors are larger at longer times compared to those for numCNN which exhibits pronounced errors at the beginning, yet these diminish significantly with time, ultimately yielding more accurate long-term predictions than anCNN. One can readily notice, from the mean squared error reported in Table 3, that numCNN learns the target weights with lower MSE. To highlight the model's precision when trained on the analytical solution versus the numerical solution, the weights in this table are shown up to eight decimal places.

Case (single)	Target Weight ($\tilde{\mathbf{b}}$)	Learned Weight ($\tilde{\mathbf{k}}_D$)	MSE (ℓ)
anCNN	—	1.09673750	$\mathcal{O}(10^{-7})$
	—	-2.19871980	
	—	1.09427700	
numCNN	1.00000000	1.00002768	$\mathcal{O}(10^{-12})$
	-2.00000000	-1.99997274	
	1.00000000	1.00002768	

Table 3: Comparison of target and learned weights for anCNN and numCNN single reference cases.

After analysing the reference case analytically in section 4.2, we progressively raise the complexity of the dataset, i.e., by setting the boundary conditions to (i) zero, (ii) finite values, (iii) randomly mixing the initial and boundary conditions, and (iv) mixing data from both Couette flow and Stokes' second problem. Each of these cases are elaborated in the subsequent sections.

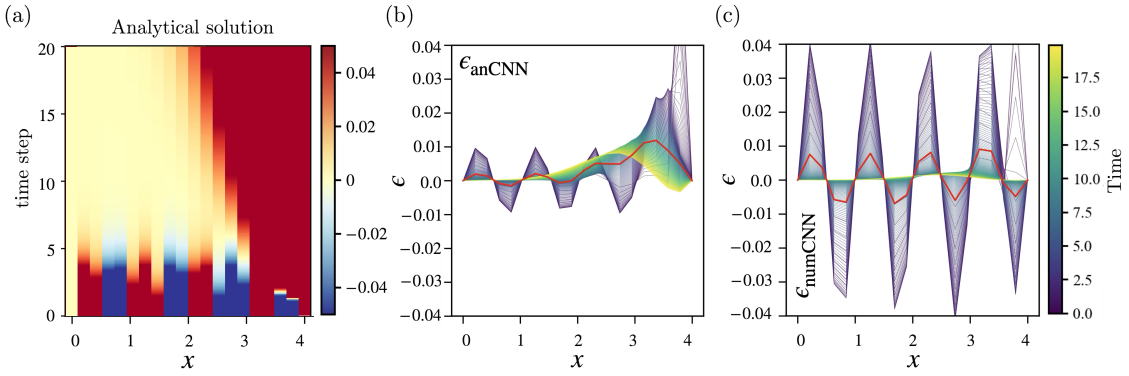


Figure 7: Comparison of CNN kernel training against the analytical solution for Couette flow $bBC = 0.0$, $tBC = 1.0$ and $u_0 = \sin(2.0\pi x)$. (a) Analytical (exact) solution for Couette flow. The error curves (difference between the analytical solution and the solution obtained from the CNN models) at different timesteps for CNN trained on (b) analytical data, and (c) numerical data. The color bar at the far right denotes time and applies to both these panels. The red curve in both panels denotes the error when time-averaged over the entire simulation. The simulation parameters used are: $\mu = 0.02$, $\Delta t = 0.1$, $n_x = 20$, $L_x = 4.0$, $N_t = 200$, $\Delta x = L_x/(n_x - 1)$.

4.2.2 Zero Boundary Conditions: $u(0, t) = 0, u(L, t) = 0, u(x, 0) = \sin(0.5\pi x)$

The analytically trained CNN (anCNN) model is tested against a number of cases of homogeneous Dirichlet (zero) boundary conditions, each having randomly initialised weights. The initial condition is chosen as a single repeating sine function over the domain, and set to zero at each boundary. Table 4 reports the final set of learned weights alongside the three fundamental criteria for classical numerical-schemes, i.e, consistency, symmetry, and stability (CFL). Following equations, (7a, 7b and 7c), consistency requires the sum of the three weights to be zero, symmetry requires the weights u_{i-1} and u_{i+1} to be equal, and stability requires that the CFL condition is met. Please note, although the second column of Table 4 shows the learned weights only to two decimal places for the sake of brevity, the model was trained to high precision with each of the weights available up to eight decimal places. Seen from the table, *Runs* 1 to 4, while failing to satisfy consistency and stability, each of them successfully satisfies the symmetry criterion, with *runs* 1 to 3 having an approximate symmetry value almost zero (0.01). This indicates that even without any explicit constraint, the model captures the inherent symmetry of the data.

The systematic violation of consistency and CFL-stability across all four runs can be attributed to two factors. First, zero Dirichlet boundaries provide no informative gradient at the edges. A diffusion process simply moves a signal to zero, a process that may not need a consistent stencil. Thus, leaving the CNN kernel learner with too weak a signal to train on near the domain limits. Second, random weight initialisation permits convergence to various symmetric stencils that fit the data numerically but do not capture physical consistency. Notably, failure to converge to $[1, -2, 1]$

Run	Learned Weights (\tilde{k}_D)	Consistency	Symmetry	Stability (CFL)
1	[0.14, -0.38, 0.15]	\times (-0.09)	\times (0.01)	\times (1.71)
2	[0.09, -0.28, 0.10]	\times (-0.09)	\times (0.01)	\times (1.81)
3	[0.13, -0.36, 0.14]	\times (-0.09)	\times (0.01)	\times (1.73)
4	[-0.04, -0.03, -0.04]	\times (-0.11)	\checkmark (0.00)	\times (2.08)
5*	[1.00, -2.00, 1.00]	\checkmark (0.00)	\checkmark (0.00)	\checkmark (0.00)

Table 4: Learned weights for zero boundary condition with random initial weights. A checkmark (\checkmark) indicates the condition is satisfied, to 2 decimal places, and a cross (\times) indicates it is not. The values in brackets next to the three conditions are to quantify the \checkmark and \times for all runs made. Criteria for these marks follow that the three conditions are satisfied per the equations : (1) Consistency: $\tilde{k}_{D-1} + \tilde{k}_{D0} + \tilde{k}_{D+1} = 0$, (2) Symmetry: $\tilde{k}_{D+1} - \tilde{k}_{D-1} = 0$ and (3) Stability (CFL): $2 - (\tilde{k}_{D-1} + \tilde{k}_{D+1}) = 0$. (*) — Run 5 has PINNs (Eq.7a),(Eq.7b) and (Eq. 7c) enforced with $\lambda_1, \lambda_2, \lambda_3 = 0.1$.

was observed with these boundary conditions when trained on the numerical dataset. For run 5*, each of the constraints in Eqns. (7a, 7b and 7c) was enforced via a Lagrange multiplier, λ_n . A parametric study identified $\lambda_n=0.1$ as the most effective and appropriately soft value to bias the CNN kernel learner toward the target weights (this is elaborated in the Appendix, see Figure A1 which summarises the results supporting this selection).

It is observed that the activation of all the constraints efficiently guide the model towards the target weights, [1.00, -2.00, 1.00]. Interestingly, the stability constraint ($\lambda_3 = 0.1$) alone proves sufficient to guide the model towards the target weights. This implies that the consistency and symmetry constraints are already mostly learnt from the data, supported by near zero consistency and symmetry values in table 4 for runs 1-4.

4.2.3 Finite Boundary Conditions: $u(0, t) = 0, u(L, t) = 1, u(x, 0) = \sin(0.625\pi x)$

The CNN model is now applied for Couette flow with top wall sliding (and fixed bottom wall) as contrasted to the fixed (both top and bottom) wall boundary conditions discussed in section 4.2.2. The initial condition of a sine function with $1\frac{1}{8}$ period was kept unaltered to match the zero velocity at the bottom boundary, and the maximum velocity at the top boundary, i.e., [0,1]. This to ensure that the solution is smooth in both space and time. When a sliding wall boundary condition is imposed instead of a zero boundary condition, the model readily satisfies all three numerical scheme conditions (Eqns. 7a, 7b and 7c) under the given initial condition. Random initial weights were assigned to each case, and the specification of the finite boundary condition introduced a ‘soft bias’ in the learning process. This highlights the sensitivity of the CNN kernel learning process to the imposed boundary conditions. Without any additional constraints, the model consistently

produces the learnt weights $[0.99, -1.98, 0.99]$ across six independent runs. This gives an indication of how close this case learns weights very close to the numerical solution. These weights satisfy all three conditions: consistency (0.00), symmetry (0.00), and stability (0.02). Subsequently, PINNs constraints are applied. A Lagrange multiplier $\lambda_n = 0.1$ is activated for all three constraints ($\lambda_1, \lambda_2, \lambda_3$) across six runs. The resulting learnt weights $[1.00, -2.00, 1.00]$ again satisfies all three conditions [(1) Consistency: $\tilde{k}_{D-1} + \tilde{k}_{D0} + \tilde{k}_{D+1} = 0$, (2) Symmetry: $\tilde{k}_{D+1} - \tilde{k}_{D-1} = 0$ and (3) Stability (CFL): $2 - (\tilde{k}_{D-1} + \tilde{k}_{D+1}) = 0$]: consistency (0.00), symmetry (0.00) and stability (0.00), reproducing the numerical weights. Finally, comparison of error metrics shows that the mean squared error (MSE) in the learnt weights obtained by anCNN is larger than that of numCNN (10^{-7} vs. 10^{-12}), as reported in table 3. This discrepancy is attributed to the attempt to use a second-order accurate three-point stencil to approximate the full analytical solution.

4.2.4 Energy (or, loss) landscape of the solution:

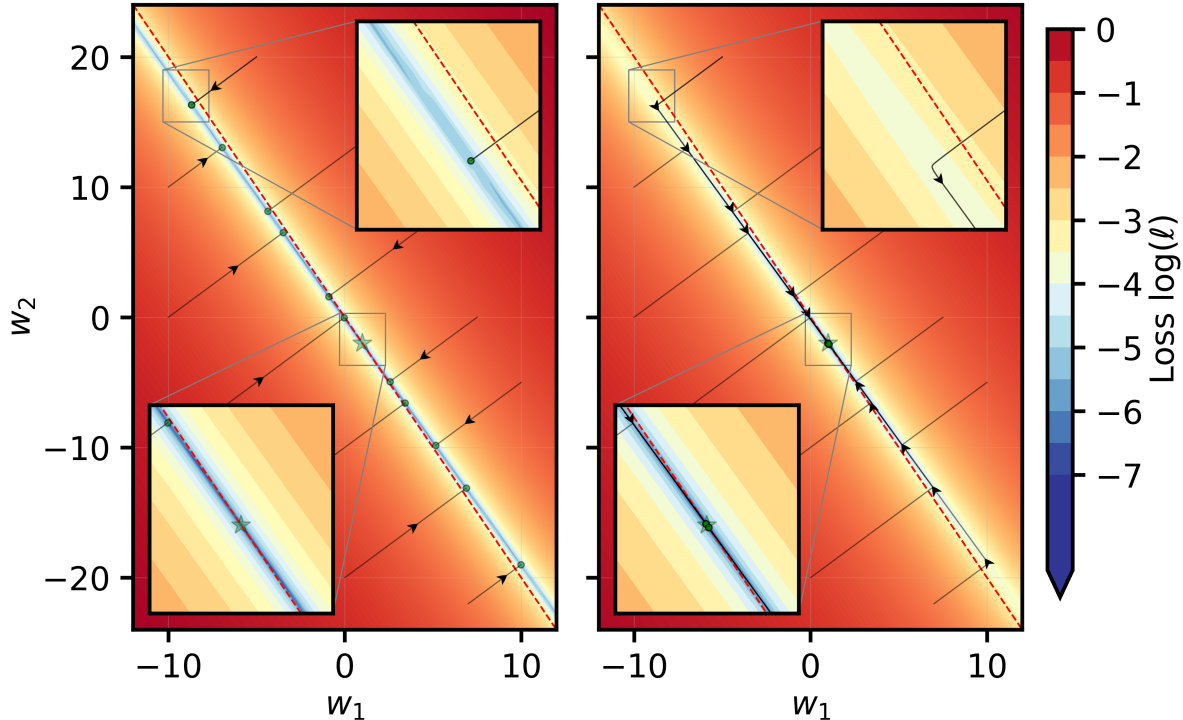


Figure 8: Contour plots showing energy landscape, generated by grid of sampled w_1 and w_2 values, assuming $w_3 = w_1$ ($w_1 = \tilde{k}_{D-1}$, $w_2 = \tilde{k}_{D0}$ and $w_3 = \tilde{k}_{D+1}$) and calculating cumulative loss over 200 single steps starting from analytical value at t and predicting $t + 1$ numerically using these weights. Left : zero boundary conditions of section 4.2.2; right : finite boundary conditions of section 4.2.3

To better understand the optimisation process across the parameter space in 4.2.2 and 4.2.3,

we adopt the idea of energy (or, MSE (ℓ)) landscape where a high energy (loss) means further away from the optimal solution, while the lowest energy corresponds to stable solutions. Fig. 8 shows the energy (loss) landscape as a function of the parameters learned weights w_1 and w_2 with the assumption that $w_1 = w_3$, as expected for symmetry. Each point on the map represents a specific combination of these w_1 and w_2 , and the colour indicates the logarithmic loss scale. Blue regions (which would take the form of valleys in a 3D plot) correspond to low loss indicating most stable states, while red regions (would take the form of peaks in a 3D plot) indicate unstable states. A series of training trajectories are shown with initial values of $w_1 = w_3$ and w_1 vs w_2 values chosen to cover the space. Arrows show how a solution approaches the stable configurations.

The left panel of Fig. 8 shows loss landscape corresponding to the case with zero boundary condition as discussed in section 4.2.2, i.e., $u(0, t) = 0$, $u(L, t) = 0$, $u(x, 0) = \sin(0.50\pi x)$. Whereas, the right panel shows the case with finite boundary conditions discussed in section 4.2.3, i.e., $u(0, t) = 0$, $u(L, t) = 1$, $u(x, 0) = \sin(0.625\pi x)$.

4.2.5 The random mixing of initial and boundary conditions

Having studied zero and finite conditions with randomised initial weights training, the CNN model is now tested for analytical solutions with complete randomisation of the initial and boundary conditions. Specifically, all permutations of boundary values tBC and bBC, were from [-1, 0.5, 0, 0.5, 1]. The initial sine function is chosen to satisfy the boundary conditions, top and bottom boundary conditions (tBC, bBC) over the domain length L_x . The result is of form $B \sin(a\pi x - b)$. The CNN kernel learner was trained using samples drawn from the specified ranges for both boundary conditions and initial conditions; for each training data, a random boundary condition and a random initial condition were selected from those ranges. 75 different cases were conducted for this section, hence having 75 different learnt weights shown in figure 9. Out of the 75 cases, 5 cases are highlighted in Table 5.

Case	bBC	tBC	Initial condition	Learned weights (\tilde{k}_D)	Consistency	Symmetry	Stability (CFL)
1	0.0	1.0	$0.0 \sin(0.0\pi x - 0.0)$	[0.39, -1.27, 0.77]	$\times (-0.11)$	$\times (0.38)$	$\times (0.84)$
1*	1.0	0.0	$0.0 \sin(0.0\pi x - 0.0)$	[0.77, -1.27, 0.39]	$\times (-0.11)$	$\times (-0.38)$	$\times (0.84)$
2	0.5	1.0	$0.0 \sin(0.0\pi x - 0.0)$	[0.85, -1.71, 0.87]	$\times (0.01)$	$\times (0.02)$	$\times (0.28)$
3	0.5	1.0	$\sin(0.583\pi x + 0.524)$	[0.98, -1.97, 0.98]	$\times (-0.01)$	$\checkmark (0.00)$	$\checkmark (0.04)$
4	-1.0	0.0	$\sin(1.125\pi x - 1.571)$	[1.03, -2.06, 1.03]	$\checkmark (0.00)$	$\checkmark (0.00)$	$\times (-0.06)$

Table 5: Learned weights and property evaluations under mixed boundary and initial conditions. A check mark (\checkmark) indicates the condition is satisfied and a cross (\times) indicates it is not. These three conditions are satisfied (\checkmark) by the following : (1) Consistency: $\tilde{k}_{D-1} + \tilde{k}_{D0} + \tilde{k}_{D+1} = 0$, (2) Symmetry: $\tilde{k}_{D+1} - \tilde{k}_{D-1} = 0$ and (3) Stability (CFL): $2 - (\tilde{k}_{D-1} + \tilde{k}_{D+1}) = 0$. bBC = bottom boundary condition; tBC = top boundary condition.

In case 1, an asymmetric stencil emerges when the system is initialised with zero initial conditions. This is start-up Couette flow, a very common test case in fluid dynamics and relevant for

many areas such as tribology or jet coating. Under these settings, the CNN kernel does not learn a stencil near to the numerical weights [1,-2,1]. Instead, the model repeatedly converges to the same one-sided stencil reported in table 5. This stencil is obtained for many independent initial weights even initial weights [1,-2,1]. This one-sided stencil is attributed to the impulse started nature of the flow from a zero initial condition, which results in a discontinuity at time zero next to the wall. There is a resulting error in the numerical scheme which cannot capture this discontinuity. As a result, the optimal stencil to reduce this error appears to be the one obtained which does not satisfy symmetry. Interestingly, when the boundary conditions are flipped (i.e., $bBC = 1, tBC = 0$) while keeping the initial condition unchanged, the CNN kernel learns weights of $[0.77, -1.27, 0.39]$, which represents a reversed form of the earlier stencil. This is represented as case 1* in table 5 and figure 9. This reversal demonstrates potential bias in ML model due to one-sided datasets. One way to fix this is to train on multiple datasets, here Cases 1 and 1* were jointly trained as a single scenario, referred to as case 1mix, to examine how the model integrates information from both. The resulting learned weights from case 1mix are $[0.8669979, -1.718784, 0.8669848]$ showing the asymmetry is removed on average, but the resulting solution is not simply the general one from the numerical solver. Another approach is to use Physics-Informed Neural Networks (PINNs). PINNs, when activated for all three constraints gives learnt weights $[0.99953544, -1.9975013, 0.99878305]$ close to the expected generalised form. This outcome demonstrates that although both original cases individually produced incorrect weights, their combination enabled the model to converge more closely toward the target weights and that adding PINNS gets a solution which matches the general numerical form. With symmetry (λ_2) enabled, case 1 matches case 1mix. Only the stability term (λ_3) drives convergence, as also seen in Section 4.2.2.

For case 2, the learnt weights deviate significantly from the expected target weights. Similar to case 1, this scenario is also initialised with a zero initial condition, as shown in table 5. Repeated runs with randomised kernel weights consistently converge to the same set of weights. When the boundary conditions are flipped ($bBC = 1, tBC = 0.5$), the learnt weights (w_1 and w_3) also flip, mirroring the behaviour observed in case 1. This again underscores the strong role of boundary conditions in shaping the learning process.

In case 3, the CNN kernel consistently converges towards the prescribed set of weights, even after four repeated runs. This case demonstrates how continuous initial condition tend to provide a smooth learning process, guiding the kernel towards repeatable convergence. Case 4 shows a scenario where the learned weights are greater than the target weights for a defined boundary condition and initial condition.

However, for all five cases in table 5 trained on numerical solution converges towards the target weight $[1, -2, 1]$. This reinforces the discussion done in section 4.1 which identifies the numCNN as the most general solution. Figure 9 highlights the weights from the 75 cases run made for section 4.2.5 and other *cases* defined in its caption.

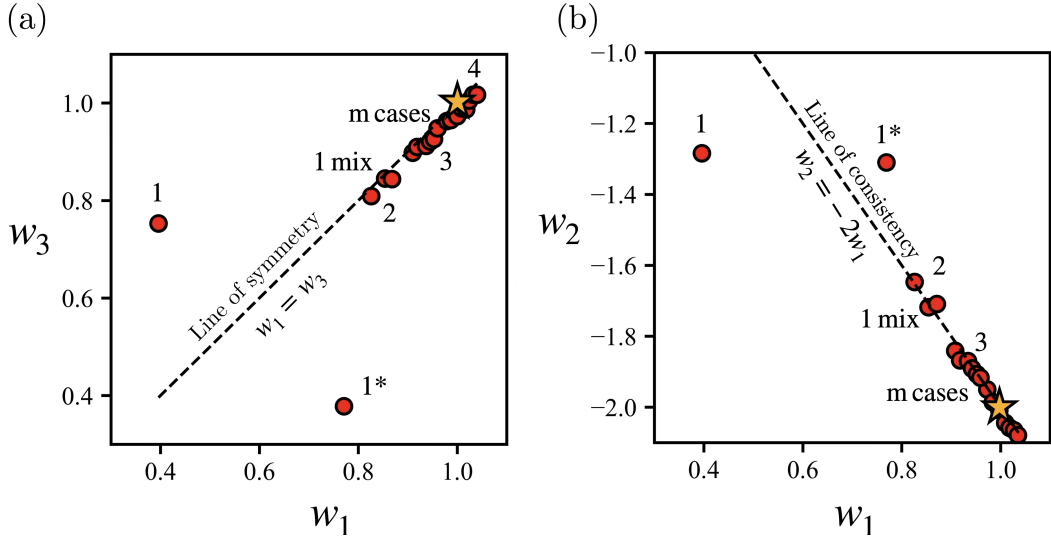


Figure 9: Scatter plot showing exploration of possible scenarios in the w_1-w_3 and w_1-w_2 ($w_1 = \tilde{k}_{D-1}$, $w_2 = \tilde{k}_{D0}$ and $w_3 = \tilde{k}_{D+1}$) parameter spaces, emphasising cases 1, 1^* , 2, 3, 4 and 1mix which are discussed in section 4.2.5 (table 5), and ‘m cases’ (combined multi case) as in section 4.2.6. The star symbol denotes the target numerical weights [1, -2, 1].

4.2.6 Combining data from Couette flow and Stokes’ second problem

A combined multi-case problem is analysed, unifying many of the studies so far, including cases which give asymmetric weights or fail to converge to the general [1, -2, 1] case. We already observed that mixing cases, as shown in case 1mix ($1 + 1^*$) in section 4.2.5, removes systematic bias in the training. This has deep analogies in both ML in general and fluid dynamics where datasets must be diverse and representative of the potential scenarios. For this case, the FE3 CNN kernel learner is trained on a combination of two Couette flow and four Stokes’ second problem, as summarised in Table 6.

Analytical settings similar to previous ones were used to train the model, with the exception that training was carried out in batches. This is due to the dataset being large (1,194 samples) as compared to previous cases. The model was trained for 1,000 epochs with Adam optimizer; learning rate was 10^{-3} , with no weight decay. Weights were initialised by employing Xavier (Glorot) algorithm, and all cases were shuffled together before training to avoid any order-dependent pattern. Batching improved memory, compute efficiency and averaged gradients per batch, which stabilized updates, while the added noise helped generalisation.

We observed that the model learns the kernel weights as illustrated in Fig.10 a. The corresponding weights are [0.99507344, -1.9861549, 0.9918588]. Consistency (0.00), symmetry (0.003), and CFL-stability (0.013) are simultaneously satisfied. This confirms that training on a dataset that covers a variety of cases, provides the model with sufficient information to recover the exact

Flow field	tBC	bBC	ω	Initial condition
(a) Couette flow	0	1	0	$\sin(0.625\pi x)$
(b) Couette flow	1	0	0	$\sin(0.625\pi x + \pi/2)$
(c) Stokes' 2 nd Problem	$\sin\omega t$	0	0.5	$-A \exp(-\kappa x) \sin(\kappa x)$
(d) Stokes' 2 nd Problem	$\sin\omega t$	0	1.0	$-A \exp(-\kappa x) \sin(\kappa x)$
(e) Stokes' 2 nd Problem	0	$\sin\omega t$	0.5	$-A \exp(-\kappa x) \sin(\kappa x)$
(f) Stokes' 2 nd Problem	0	$\sin\omega t$	1.0	$-A \exp(-\kappa x) \sin(\kappa x)$

Table 6: Flow conditions used to generate the dataset for combined training. Here $\kappa = \sqrt{\omega/(2\mu)}$, bBC and tBC denote the bottom and top boundary conditions, respectively.

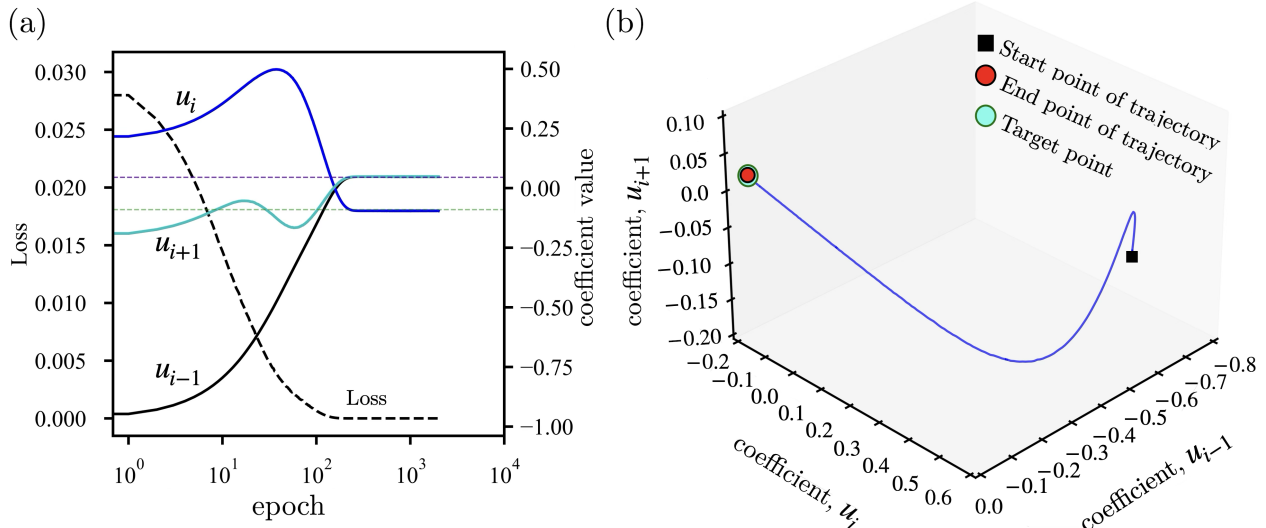


Figure 10: (a) Loss plot and convergence for complementary mixed flows (wall-driven flow, and stokes second problem). The coefficients are in the form of k_D . (b) 3D visualisation of training from start to end for a mixed (wall driven flow and stokes second problem) case.

physics-preserving kernel. Overall, exposing the model to balanced flow cases and appropriate boundary conditions effectively constrains training, guiding the CNN to infer target weights that meet all numerical-scheme criteria.

4.3 Comparison between numCNN and anCNN

The preceding discussions on the performance of the two operator learning strategies, i.e., numCNN and anCNN, clearly demonstrate a major difference between the methods' generalisation ability.

The numCNN is shown to give exact agreement to the numerical stencil, an expected result given the mathematical form of the CNN is identical to the finite difference stencil. Numerical data implicitly carry information concerning numerical discretisation, as such numCNN inheres this from the training data. For a 3 point stencil (as well as 5 point and multi-step Adam-Bashforth), the numCNN model can be viewed as the most *generalised* form a CNN can be, given it could be applied to any boundary condition or geometry yielding consistent results. The agreement between the numCNN and the numerical stencil reassures this point, and represents a major advantage of using simple NN to avoid black box behaviour.

When trained on the analytical form Eq. 2, an exact solution of the differential equation, the 3 point numerical stencil of the anCNN is only able to approximate this solution. However, this 3 point stencil trained in this way is potentially more *accurate*, as a result of being overtrained on a particular analytical case. The consequence of this overtraining is that the anCNN is indeed not expected to generalise to another case, since it is pertinent only to the original flow field. Consequently, when solving flows that span a wider range of parameter space, and therefore produce substantially different flow physics (see Section 4.2.6 for the Couette flow and Stokes' second-problem cases), numCNN demonstrates greater generalisability than anCNN as seen in section 4.1.1. Accordingly, anCNN performs well on balanced flow cases but requires more exposure to varied flow regimes and carefully chosen boundary conditions to match numCNN's generality.

In some cases, such as a pure diffusion problem in the absence of boundary conditions, the anCNN fails to train the model to a consistent set of weights. This is attributed to the under-defined nature of the problem where any operator could take an initial condition and move it towards zero. Hence, enforcement of additional constraints, or PINNs is required to recover a consistent stencil. In particular the stability condition of Eq 7c which indirectly enforces a viscosity magnitude on the problem, results in the expected weights from the numerical scheme. This trade-off between the general numCNN and accurate anCNN has deep parallels to the field of machine learning in physics, where complex architectures struggle to generalise beyond the training dataset (Yuan et al., 2022) with PINNs helping to expand generalisability by embedding physics and so requiring less data (Raissi et al., 2019).

4.4 mdCNN: Trained on Molecular Dynamics Simulations

The training of CNNs on both analytical and numerical solutions demonstrate the effectiveness of CNNs in solving differential equations. As opposed to other forms of Artificial Neural Networks (ANNs), the use of convolutional neural networks incorporates the spatial information of the physical problem. Hence, any variation in the local velocity field is automatically accounted for. This section examines whether a CNN can leverage spatial locality to predict flow fields with rich local variations described by a fundamentally different governing equation of Molecular Dynamics (MD) simulations.

The uniqueness of MD is that it does not require us to simulate the diffusion equation, nor does it require the assumptions of the transport coefficients (e.g., viscosity, surface tension, conductivity); instead these properties and the flow field itself, emerge naturally as average observations of

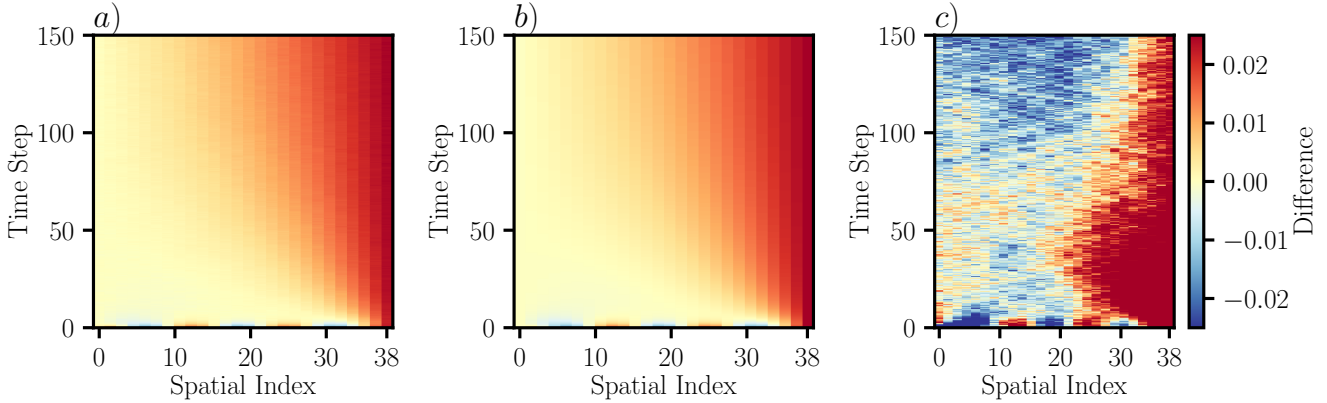


Figure 11: MD vs trained model with *a*) the MD time space plot over 3000 timesteps of size 0.05, with model trained in *b*) where weights are $[0.984, -1.96, 0.976]$ and difference between the model and MD in *c*) showing the extra physics in the MD simulation not captured by the mdCNN, which includes both noise as well as an apparent signal, which may indicate local viscosity variation, near the top boundary.

the motion of thousands or millions of particles. The solving of fluid dynamics with molecules, known as Non Equilibrium MD (NEMD), has been shown to reproduce a wide range of fluid phenomena (Rapaport, 2004; Todd and Daivis, 2017). As a result, it is closer to running an experiment and taking observations of the collective behaviour of the particles. For this reason, MD provides an excellent test of the limits of employing CNN for ML driven flow modelling. The measured velocities include noise, with the average velocity known to broadly agree with the unsteady diffusion equation with what can be interpreted as additional fluctuations (Sprittles et al., 2023; Zhang et al., 2019). These noise terms can be seen in Figure 11 with the difference between the predicted flowfield from the mdCNN trained on the MD data. The training is performed only for cells in the fluid region (the 26 bins not including tethered wall atoms), with the CNN trained on $n_x = 28$ cells with bottom and top set to boundary conditions ($u(0, t) = 0$ and $u(L_y, t) = 1$) respectively. The resulting mdCNN has weights of $[0.984, -1.96, 0.976]$ assuming a viscosity $\mu = 2.14$ as in the matched analytical solution of Figure 3, a value consistent with previous work (Smith, 2013). The loss drops to order 10^{-6} which gives consistency (0.00), symmetry (-0.008), and stability $2C - \sum_{i=1}^3 i^2 k_i^2 = 0.04$. However, starting the training from random initial weights can result in variation in final weights, some of which give an unstable numerical solvers, e.g. $[1.085, -1.860, 1.077]$. This can usually be fixed with careful choice of training algorithm, varying training rates or inclusion of a scheduler.

However, this approach could also be employed to solve the so-called inverse problem, where Δx and Δt are prescribed, and the deviation of the obtained weights from the numerical set $[1, -2, 1]$ allows an estimate of the effective viscosity in the MD system. This provides an alternative route to the various schemes of obtaining viscosity in MD, including Green Kubo and other NEMD

methods (Evans and Morris, 2007). Because the fit uses the entire time and space response of the NEMD system, and given the robust nature of the ML training algorithms, it would be expected to provide a fairly reliable way to judge viscosity. In addition, the process could be extended to more complex physics by modelling additional terms, for example the CNN approach is known to work with convective and diffusive terms (Queiruga, 2019), identifying both individually. This also points to the tantalising possibility of training when the appropriate PDE is unknown, providing the numerical kernel of potential differential terms in CNN form and observing which terms are non-zero after training. This has similarities to pySindy (Brunton et al., 2024) but replacing functional forms with CNN weights, driven by the ML backpropagation algorithm, may potentially allow more robust equation identification. It also remains to be seen how resistant to noise the methodology will be, as the current case is extensively averaged to give a very low noise to signal ratio, as can be observed by the agreement between analytical and MD profiles in Figure 3 as well as 11a) and 11b).

5 Conclusion

This study integrated machine learning with computational fluid dynamics by utilizing convolutional neural network (CNN) kernels as numerical operators. The proposed framework requires considerably fewer trainable parameters than traditional data driven approaches without compromising the accuracy and reproducibility of the flow-field. The learnt CNN kernels are mathematically identical to the finite difference operators, which resolves the ‘black box problem’. Two benchmark problems, i.e., wall-driven (Couette) flow and Stokes’ second problem illustrate the implementation and efficacy of these CNN-based schemes. A dedicated “CNN kernel learner” was trained on finite-difference solutions (numCNN) to recover the exact stencil coefficients, achieving consistent convergence regardless of random initialisation. The CNN kernel learner (numCNN) accurately inferred the expected flow fields when applied to unseen conditions, demonstrating robust generalisation (Section 4.1.1). The performance of the CNN kernel learner trained on analytical solutions (anCNN) was evaluated across cases with increasing complexities, as detailed in Section 4.2. In some cases, such as zero boundary conditions, the kernel fails to repeatably find a unique numerical operator. In other cases, the learnt operator is different from the general numerical operator and for extreme cases, the training data can result in skewed and unphysical kernels. The simple nature of the CNN kernel means we retain clear insight into the limitation of the training approach, with symmetry or consistency violated in the operator despite the resulting flow fields still appearing to provide reasonable agreement with expected behaviour. These cases can be reduced by mixing a wider range of training data from various problems or applying known physics through Physics-Informed Neural Network (PINNs) like constraint terms. This provides deep insights into the limitation of data driven fluid dynamics, namely the requirement for balanced and diverse datasets and application of physics when this is not possible. Section 4.2.6 highlights the significant impact of training data composition on the learning performance of the CNN kernel learner. Training on a mixed and well-balanced set of analytical solutions notably

enhances the model’s ability to generalise. This improved generalisation is further demonstrated through the application of the CNN kernel learner to molecular dynamics data (mdCNN), where the model effectively learns approximate target weights despite the inherent noise in MD datasets. These results confirm the robustness and adaptability of the framework across both structured and noisy data environments.

Overall, the results demonstrate the promise of CNN-based differential operators for both numerical and analytical settings. When trained on numerical solutions, the CNN kernel learner reliably recovers the target finite-difference weights; when trained on analytical data, the outcome is sensitive to the composition of the training set, so well-designed and balanced datasets are required to guide the model toward the correct weights. Tests with MD simulations reinforces that this simple convolutional operator can extract meaningful operator weights even from noisy data. Together, these findings support the view that machine learning can produce interpretable, engineering-compatible finite-difference operators rather than opaque “black boxes”. These interpretable operators can discover coefficients through the inverse problem and even determine differential equations. The findings of this work may serve as the ground work for future studies extending the proposed approach to experimental and higher-fidelity simulation data, explore non-linear flow regimes and operator stability, and evaluate alternative hybridisation strategies and ML architectures to broaden robustness and applicability.

6 Funding and Data Availability

Funding

This work was supported by the EPSRC ref. EP/W524542/1

Data Availability

All simulation code and processed data are available on Github under [kwamea-b/CNN_numerical_schemes](https://github.com/kwamea-b/CNN_numerical_schemes).

A Appendix

A.1 Forward Euler 5-point stencil

A similar approach for discretisation is taken for the forward Euler 5-point as done in equations 4 and 5 above in section 3.3. However, since a 5-point stencil is discussed here the weightings and terms of k_1 changes now. Thus equations 3 and 4 changes to:

$$\frac{u_i^{t+1} - u_i^t}{\Delta t} = \mu \left(\frac{-u_{i-2}^t + 16u_{i-1}^t - 30u_i^t + 16u_{i+1}^t - u_{i+2}^t}{12(\Delta x)^2} \right) \quad (11)$$

$$u_i^{t+1} = C(-u_{i-2}^t + 16u_{i-1}^t - 30u_i^t + 16u_{i+1}^t - u_{i+2}^t) + u_i^t \quad (12)$$

where,

$$C = \frac{1}{12} \frac{\mu \Delta t}{(\Delta x)^2} = \text{constant} \quad (13)$$

A.1.1 Boundary Conditions Handling: Mirroring Approach

For this numerical-scheme operator, a mirroring approach is applied to handle the boundary conditions instead of using a one-sided stencil. This choice avoids any modification to the convolution kernel. In practice, ghost cells are generated at each boundary by reflecting the adjacent interior values across the boundary: the right-hand ghost cell is obtained by mirroring its neighbouring interior point about the right boundary, and the left-hand ghost cell is generated similarly at the left boundary. The mirroring procedure is expounded below. As defined earlier the boundary condition used here are Dirichlet boundary conditions:

$$bBC = u(0) = 0 \text{ & } tBC = u(L) = 1$$

Two ghost cells are needed on the left side of the boundary domain, denoted u_{l1} and u_{l2} to compute a 5-point stencil at the first interior point. The mirroring approach sets out these ghost cells by reflecting interior values u_1 and u_2 about the boundary location. The boundary value bBC is to lie halfway between the ghost cell and its corresponding interior cell.

$$\text{For ghost cell 1 } (u_{l1}) : \quad bBC = \frac{u_{l1} + u_1}{2} \quad (14)$$

$$\text{For ghost cell 2 } (u_{l2}) : \quad bBC = \frac{u_{l2} + u_2}{2} \quad (15)$$

which can be rearranged to compute the ghost cells. A similar approach can be employed for the top boundary condition (tBC) reflecting the last and second to last to last to interior values, u_N and u_{N-1} respectively.

For both boundaries, the mirroring is exactly implemented in the code as well. The ghost cells are concatenated with the interior values to form an extended array (padded tensor) over which convolution i.e. finite difference update is performed. In this way, the approach is valid for CNN, and can be extended to arbitrary order stencils/kernel sizes. The mirroring approach allows for the finite difference stencil (5-point) to remain centred hence maintaining the accuracy of the scheme near the boundaries as well as satisfying the boundary conditions.

A.2 Adams Bashforth

The Adams Bashforth 2nd order is a multistep method taking into account discretising in both temporal and spatial space. Below is the equation for Adams Bashforth 2nd order.

$$u_i^{t+1} = u_i^t + \frac{3}{2} H_i^t - \frac{1}{2} H_i^{t-1} \quad (16)$$

A.2.1 3-point stencil

For the 3 point stencil, the operator is,

$$H^n(u) = C(u_{i-1}^n - 2u_i^n + u_{i+1}^n), \quad (17)$$

which can give the current ($n=t$) and previous $n=t-1$) timesteps. For equation (16), the model uses two convolution layers. Thus, one for the current time step and another for the previous timestep. A forward Euler is performed initially to "bootstrap" the system. Bootstrapping is used here as Adams–Bashforth 2nd order is a multi-step method where the scheme requires two past states u^t and u^{t-1} to obtain the next state u^{t+1} . Both current (n) and previous timesteps ($n-1$) are represented by two kernels in the code. These are taken in and passed in as 2 channel input where the next state is obtained. However, functionally this could also be treated as a 2×3 spatio-temporal stencil. The Adams Bashforth model is iterated over time where the two convolutional layers (previous and current) are updated. After, the boundary conditions are explicitly re-imposed again so the boundary conditions are satisfied.

A.2.2 5-point stencil

When the stencil is a 5-point stencil,

$$H^n(u) = C \left[\frac{-u_{i-2} + 16u_{i-1} - 30u_i + 16u_{i+1} - u_{i+2}}{12} \right] \quad (18)$$

with overall time step as in (16).

The model uses two convolution layers, one for current timestep and another for previous timestep. Bootstrapping is used here as well as it is a multistep method. The mirroring approach is also needed as it is a 5-point stencil. Ghost cells are created to ensure that the results stay consistent and to ensure the boundary conditions are handled properly.

A.3 PINNs constraints study

A parametric study using PINNs identified $\lambda_n = 0.1$ as the optimal Lagrange multiplier to guide the CNN kernel toward the target weights. Error magnitude, ϕ was measured between learned L and target T weights, i.e. computed as $\phi = \sqrt{(L_1 - T_1)^2 + (L_2 - T_2)^2 + (L_3 - T_3)^2}$ and results showed that for $\lambda_n \geq 0.1$, both boundary conditions (ZBC and FBC) converged with minimal error. Thus, $\lambda_n = 0.1$ was chosen to ensure effective PINNs activation. This studies is seen in figure A1 indicating the error analysis conducted.

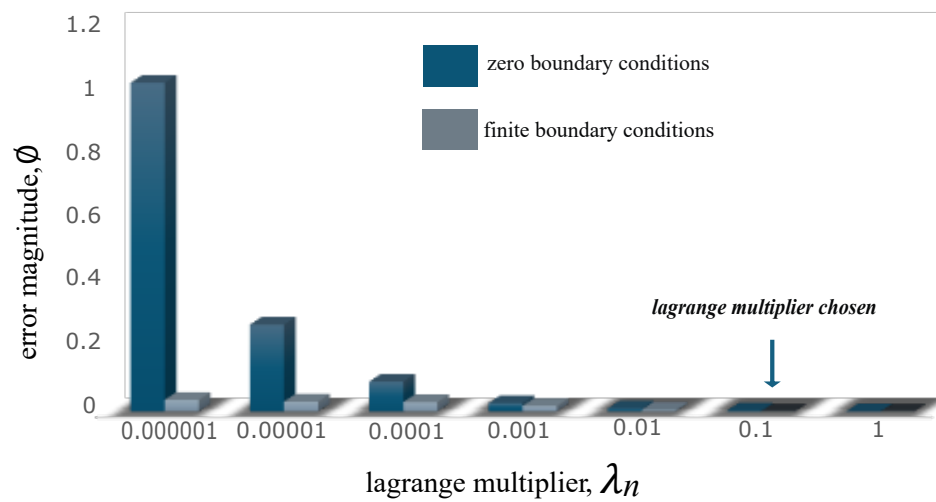


Figure A1: Parametric studies plot done for the selection of lagrange multiplier(λ_n) using cases (i)zero boundary conditions and (ii)finite boundary conditions on a range of values.

References

L. Agostini. Exploration and prediction of fluid dynamical systems using auto-encoder technology. *Physics of Fluids*, 32(6), Jun. 2020. doi: 10.1063/5.0012906.

Viktor Ambarzumian. Über eine frage der eigenwerttheorie. *Zeitschrift für Physik*, 53:690–695, 1929. doi: 10.1007/BF01330827. URL <https://doi.org/10.1007/BF01330827>.

Andrea Bonfanti, Roberto Santana, Marco Ellero, and Babak Gholami. On the generalization of pinns outside the training domain and the hyperparameters influencing it. *Neural Computing and Applications*, 36(36):22677–22696, 2024.

S.Ł. Brunton, B.Ŕ. Noack, and P. Koumoutsakos. Machine learning for fluid mechanics. *Annual Review of Fluid Mechanics*, 7, 2024. doi: 10.1146/annurev-fluid-010719. Downloaded from www.annualreviews.org.

John WM Bush. The new wave of pilot-wave theory. *Physics Today*, 68(8):47–53, 2015.

S. Cai, Z. Wang, S. Wang, P. Perdikaris, and G.Ē. Karniadakis. Physics-informed neural networks for heat transfer problems. *Journal of Heat Transfer*, 143(6), Jun. 2021. doi: 10.1115/1.4050542.

Arthur da Cunha, Emanuele Natale, and Laurent Viennot. Proving the Strong Lottery Ticket Hypothesis for Convolutional Neural Networks. In *ICLR 2022 - 10th International Conference on Learning Representations*, Virtual, France, April 2022. URL <https://hal.science/hal-03548226>.

Z. Deng, J. Wang, H. Liu, H. Xie, B. Li, M. Zhang, T. Jia, Y. Zhang, Z. Wang, and B. Dong. Prediction of transonic flow over supercritical airfoils using geometric-encoding and deep-learning strategies. ArXiv preprint, 2023. URL <https://arxiv.org/abs/2300.00000>.

D. J. Evans and G. P. Morris. *Statistical Mechanics of Non-Equilibrium Liquids*. Australian National University Press, 2nd edition, 2007.

Lukas Fesser, Luca D'Amico-Wong, and Richard Qiu. Understanding and mitigating extrapolation failures in physics-informed neural networks. *arXiv preprint arXiv:2306.09478*, 2023.

G.Ķ. Fordjour. Development of a deep learning-based flood forecasting tool with firefly algorithm for the blackburn fork watershed, tennessee. Master's thesis, Tennessee Technological University, 2024.

Xavier Glorot and Yoshua Bengio. Understanding the difficulty of training deep feedforward neural networks. In *Proceedings of the thirteenth international conference on artificial intelligence and statistics*, pages 249–256. JMLR Workshop and Conference Proceedings, 2010.

Vikas Hassija, Vinay Chamola, Atmesh Mahapatra, Abhinandan Singal, Divyansh Goel, Kaizhu Huang, Simone Scardapane, Indro Spinelli, Mufti Mahmud, and Amir Hussain. Interpreting black-box models: a review on explainable artificial intelligence. *Cognitive Computation*, 16(1): 45–74, 2024.

C. Hirsch. *Numerical Computation of Internal and External Flows: The Fundamentals of Computational Fluid Dynamics*. Elsevier, 2007.

Y. Kim and Y. Choi. Learning finite difference methods for reaction-diffusion type equations with fcnn [formula presented]. *Computers and Mathematics with Applications*, 123:115–122, Oct. 2022. doi: 10.1016/j.camwa.2022.08.006.

Diederik P Kingma and Jimmy Ba. Adam: A method for stochastic optimization. *arXiv preprint arXiv:1412.6980*, 2014.

Yann LeCun and Yoshua Bengio. Convolutional networks for images, speech, and time series. *The handbook of brain theory and neural networks*, 1998.

Zongyi Li, Nikola Kovachki, Kamyar Azizzadenesheli, Burigede Liu, Kaushik Bhattacharya, Andrew Stuart, and Anima Anandkumar. Neural operator: Graph kernel network for partial differential equations. *arXiv preprint arXiv:2003.03485*, 2020.

Z. Long, Y. Lu, X. Ma, and B. Dong. Pde-net: Learning pdes from data. Technical report, arXiv, 2018. *arXiv:1811.xxxx*.

NIST. *SAT-TMMC: Liquid-Vapor Coexistence Properties -Linear-Force Shifted Potential at 4.0 σ* . National Institute of Standards and Technology, accessed: 2026-01-05.

K. O’Shea and R. Nash. An introduction to convolutional neural networks. *arXiv preprint*, 2015. URL <http://arxiv.org/abs/1511.08458>.

J. Petracic and P. Harrowell. The boundary fluctuation theory of transport coefficients in the linear-response limit. *J. Chem. Phys.*, 124:014103, 2006.

Alejandro Francisco Queiruga. Studying shallow and deep convolutional neural networks as learned numerical schemes on the 1d heat equation and burgers’ equation. *arXiv preprint arXiv:1909.08142*, 2019.

C. Rackauckas et al. Universal differential equations for scientific machine learning. *arXiv preprint*, 2020a. URL <http://arxiv.org/abs/2001.04385>.

Christopher Rackauckas, Yingbo Ma, Julius Martensen, Collin Warner, Kirill Zubov, Rohit Sujekar, Dominic Skinner, Ali Ramadhan, and Alan Edelman. Universal differential equations for scientific machine learning. *arXiv preprint arXiv:2001.04385*, 2020b.

M. Raissi and G. Karniadakis. Hidden physics models: Machine learning of nonlinear partial differential equations. *Journal of Computational Physics*, 357:125–141, Mar. 2018. doi: 10.1016/j.jcp.2017.11.039.

M. Raissi, P. Perdikaris, and G. Karniadakis. Inferring solutions of differential equations using noisy multi-fidelity data. *Journal of Computational Physics*, 335:736–746, 2017a.

M. Raissi, P. Perdikaris, and G. Karniadakis. Machine learning of linear differential equations using gaussian processes. *Journal of Computational Physics*, 348:683–693, 2017b.

M. Raissi, P. Perdikaris, and G. Karniadakis. Physics-informed neural networks: A deep learning framework for solving forward and inverse problems involving nonlinear partial differential equations. *Journal of Computational Physics*, 378:686–707, Feb. 2019. doi: 10.1016/j.jcp.2018.10.045.

Dennis C Rapaport. *The art of molecular dynamics simulation*. Cambridge university press, 2004.

X. Shan, Y. Liu, W. Cao, X. Sun, and W. Zhang. Turbulence modelling via data assimilation and machine learning for separated flows over airfoils. *AIAA Journal*, 61(9), 2023.

E Smith. On the coupling of molecular dynamics to continuum computational fluid dynamics. sch. *Mech. Eng*, 2013.

ER Smith, PJ Daivis, and BD Todd. Measuring heat flux beyond fourier’s law. *The Journal of Chemical Physics*, 150(6), 2019.

James E Sprittles, Jingbang Liu, Duncan A Lockerby, and Tobias Grafke. Rogue nanowaves: A route to film rupture. *Physical Review Fluids*, 8(9):L092001, 2023.

Billy D Todd and Peter J Daivis. *Nonequilibrium molecular dynamics: theory, algorithms and applications*. Cambridge University Press, 2017.

David Tong. Lectures on fluid mechanics. <http://www.damtp.cam.ac.uk/user/tong/fluids.html>, 2025. Accessed: 2025-08-14.

R. Vinuesa and S. Brunton. Emerging trends in machine learning for computational fluid dynamics. *arXiv preprint*, arXiv:2211.15145, 2022. URL <http://arxiv.org/abs/2211.15145>.

H. Wang et al. Recent advances on machine learning for computational fluid dynamics: A survey. *arXiv preprint*, arXiv:2408.12171, 2024. URL <http://arxiv.org/abs/2408.12171>.

Lingxiao Yuan, Harold S Park, and Emma Lejeune. Towards out of distribution generalization for problems in mechanics. *Computer Methods in Applied Mechanics and Engineering*, 400:115569, 2022.

Xuan Zhang, Limei Wang, Jacob Helwig, Youzhi Luo, Cong Fu, Yaochen Xie, Meng Liu, Yuchao Lin, Zhao Xu, Keqiang Yan, et al. Artificial intelligence for science in quantum, atomistic, and continuum systems. Foundations and Trends® in Machine Learning, 18(4):385–912, 2025.

Yixin Zhang, James E Sprittles, and Duncan A Lockerby. Molecular simulation of thin liquid films: Thermal fluctuations and instability. Physical Review E, 100(2):023108, 2019.